Journal of Alloys and Compounds 820 (2020) 153092

Contents lists available at ScienceDirect

Journal of Alloys and Compounds

journal homepage: http://www.elsevier.com/locate/jalcom

Effects of Cu and Zn on microstructures and mechanical behavior of the medium-entropy aluminum alloy

Bingbing Zhang [a], Peter K. Liaw [b], Jamieson Brechtl [c], Jingli Ren [d], Xiaoxiang Guo [d], Yong Zhang [a,*]

[a] State Key Laboratory for Advanced Metals and Materials, University of Science and Technology Beijing, Beijing, 100083, China
[b] Department of Materials Science and Engineering, University of Tennessee, Knoxville, TN, 37996, USA
[c] The Bredesen Center for Interdisciplinary Research and Graduate Education, The University of Tennessee, 37996–3394, Knoxville, TN, USA
[d] Henan Academy of Big Data, Zhengzhou University, Zhengzhou, 450001, China

ARTICLE INFO

Article history:
Received 31 August 2019
Received in revised form
10 November 2019
Accepted 18 November 2019
Available online 20 November 2019

Keywords:
Serration behavior
Medium-entropy alloys
Microstructure
Tensile strength
Al–Mg–Zn–Cu alloys

ABSTRACT

Lightweight alloys are becoming more and more important. Based on the 5083 aluminum alloy, the effects of Zn and Cu additions on the microstructures, properties, and serration behavior were investigated. The results show that with the increase of the Zn content, the tensile and yield strengths of the alloy increase, while the elongation and the serration amplitude keep on decreasing. Moreover, different amounts of Cu are added to the high Zn content Al–Mg-6 wt.% (weight percent) Zn alloy, in which the strength and plasticity are improved firstly. When the Cu content was 6 wt%, the elongation of the alloy is about 7%, and the serration behavior of the alloy gradually disappears. The optimal mechanical property is achieved at the composition of Al–Mg-6wt.%Zn-6wt.%Cu. The serration behavior is believed to be related to the interaction between the moving dislocations and the precipitates. Furthermore, the serrated flow was analyzed using the refined composite multiscale entropy algorithm. It was found that the dynamical complexity of the serrations generally increased with an increase in the solute density, the stress-drop magnitude, the grain size, the tensile and yield strengths, and the degree of plasticity.

1. Introduction

In the new era of the economic development, new requirements have been put forward for the energy conservation, environmental protection, safety and efficiency. Therefore, there is an urgent need to continuously improve the properties of existing materials and discover new materials.

The Al–Mg alloys have been widely used in aerospace and automotive applications due to their excellent properties, such as lightweight, corrosion resistance, weldability, and formability [1,2]. However, low strength is the main problem in the development and application of aluminum alloys. The normal methods of increasing the mechanical properties are solution strengthening, precipitation hardening, dispersion strengthening, and fine-grained strengthening [3]. As a typical representative of the Al–Mg alloy, the strength of the 5083 aluminum alloy cannot be improved by the heat treatment, but can be enhanced by solid-solution strengthening of Mg and strain hardening [4]. As a result, it is effective to further introduce solution elements to improve the strength of the 5083 aluminum alloy by means of solid-solution strengthening. In this paper, we study the microstructures and mechanical properties after adding Cu and Zn alloying elements to the 5083 alloy. After annealing, a continuous β(Al_3Mg_2) phase exists on the grain boundary. During the heat treatment, the β phase does not improve the mechanical properties and adversely affects the corrosion resistance of the 5083 aluminum alloy [5]. When Cu and Zn are added, the main phase in the alloy is η-phase ($MgZn_2$) [6], S-phase (Al_2CuMg) [7], and T-phase ($Mg_{32}(Al, Zn)_{49}$ [8], which can improve the strength of the alloy. In particular, the alloy has been changed into an alloy capable of aging strengthening. After adding Cu and Zn, the major precipitation sequence of the alloy is α (SSS) →GP→η'→η [9].

Plastic deformation is the most basic and important mechanical behavior of metallic materials. Consequently, the mechanical-instability phenomenon and the localization problem of deformation during plastic deformation have become the hot topic of plastic-deformation behavior [10]. Initially, Luders found that low-

* Corresponding author.
E-mail address: drzhangy@ustb.edu.cn (Y. Zhang).

https://doi.org/10.1016/j.jallcom.2019.153092
0925-8388/

carbon steels showed significant yielding when subjected to tensile tests at room temperature [11]. Portevin et al. found that the Al–Mg alloy exhibits a continuous repeated drop of the serration-yielding phenomenon on the stress-strain curve, which is different from low-carbon steels [12]. The plastic-instability phenomenon of alloy materials during plastic deformation is called the Portevin-Le Chatelier (PLC) effect. Currently, the reason for this phenomenon is widely recognized as the dynamic strain aging (DSA) theory proposed by Cottrell, which mainly explains the dynamic interaction between movable dislocations and solute atoms [13]. At a certain temperature and strain rate, the solute atoms can diffuse around the movable dislocation line, pinning the dislocation, and hindering their movement. When the applied stress increases to overcome this resistance, the movable dislocations will break away from the solute-atom atmosphere and continue their motion. This behavior is manifested as the serrated flow in the jerky macroscopic stress-strain curves. There are many factors affecting serrations, including the rolling reduction, strain rate, test temperature, aging, and grain size. Serrations are exhibited by a wide range of alloy materials, including low-carbon steels [14], transformation induced plasticity steel (TRIP steel) [15], high-entropy alloys (HEAs) [16–22], amorphous alloy [23][24][25][26], and so on. Furthermore, there are many studies on the effects of PLC in aluminum alloys, such as Al-Mg [27], Al-Cu [28], and Al–Li systems [29]. The study of the serration behavior in these alloy systems is of great significance since a fundamental understanding of this phenomenon can help find ways to improve the mechanical properties of the material.

Many different types of methods have been used to analyze the serrated-flow phenomenon [30–41]. For example, complexity analysis techniques have been used to investigate the serration behavior in different material systems, such as Al–Mg alloys [42,43], HEAs [40], and steels [42,44,45]. This type of measurements can gauge the degree of irregularity of the time-dependent serration behavior [46]. Thus, this type of algorithm can estimate the degree of the dynamical complexity exhibited by the serrations during the serrated-flow process.

Furthermore, previous investigations have linked the complexity of the serrations to the microstructural behavior during mechanical testing [42,44]. One investigation found that the complexity of the serrations exhibited by an Al–Mg alloy during tension were significantly lower than that of low-carbon steel [42]. The difference in the complexity values were thought to correspond to the variety of dislocation-line/solute atom interactions that could occur during deformation. For instance, the Al–Mg alloy contains substitutional atoms that can only interact with edge dislocations, whereas the interstitial carbon can interact with both screw and edge dislocations. Thus, the lower amount of interactions that occur in the Al–Mg during tension will lead to serrations that exhibit less dynamical complexity.

Another study examined the effects of carbon impurities on the complexity of the serrated flow during tension in the carburized steel [44]. Here, samples were heated in a methane containing gas at 885 °C for heating times ranging from 30 to 70 min. The increase in the heating time led to an increase in the amount of carbon impurities in the alloy. Tension testing revealed that the complexity of the serrations increased with an increase in the impurity concentration. It was theorized that the increased complexity was due to a larger number of interactions that occurred between the carbon and the dislocations during tension, resulting in more complex dynamical behavior.

At present, the PLC have been investigated extensively in the 5083 aluminum alloy [47–49]. In this paper, based on the modification of the 5083-aluminum alloy, three different alloy compositions were designed to study the effects of different alloying elements and heat-treatment processes on the mechanical properties, microstructures, and serration behavior of the alloy.

2. Experiments

2.1. Materials preparation

Based on the 5083 aluminum alloy with chemical compositions (in weight percent, wt. %) of 4.5 Mg, 0.23 Zn, 0.42 Fe, 0.57 Mn, 0.15 Cr, 0.42 Si, 0.09 Cu, and balance Al, six alloys were prepared, as shown in Table 1. 2%, 4%, 6% Zn, and 3%, 6% Cu were added to the 5083 aluminum alloy. With the addition of alloying elements, the content of Mg was gradually reduced. The raw materials were smelted, using a vacuum-induction-melting furnace to obtain ingots of three different compositions.

2.2. DSC and heat treatment

Thermal analysis was performed in a differential scanning calorimeter (DSC) to determine the approximate range of the heat-treatment temperature. The DSC samples were cut into $\phi 5 \times 1$ mm by wire-electrode cutting, and the weight between 20 and 30 mg. The samples were heated from room temperature to 700 °C in the Ar atmosphere, and the heating rate was 10 °C/min.

According to the DSC test results, the obtained ingots were homogenized at 465 °C for 24 h to modify the as-cast structure and reduce heterogeneity. Then, hot rolling was performed at 400 °C, and the amount of deformation was 80%. Finally, samples were solution treated at 500 °C for 1 h and aged at 120 °C for 24 h.

2.3. Microstructural characterization

The microstructures and compositions of the samples were analyzed by a ZEISS-SUPRA55 scanning electron microscope (SEM) with the energy-dispersive X-ray spectroscope (SEM-EDX) and Electron Backscattered Diffraction (EBSD). The samples were ground with the silicon carbide sandpaper from 1000# to 2000#. Then, the specimens were mechanically polished for the SEM observation and electrolytic polishing for the EBSD experiment. The composition of the electrolyte was 5%$HClO_4$ and 95%C_2H_5OH (weight or volume percent). The electrolytic polishing was operated at 20 V for 20–30s. The X-ray diffraction (XRD) was scanned from $2\theta = 10°–90°$ to record the XRD pattern.

2.4. Mechanical-property test

Microhardness of the sample was measured by a Vickers hardness-testing machine with a load of 200 g. The microhardness value of each sample was obtained from the average of 10 data points.

The sample was subjected to the tensile test on an electromechanical universal tensile testing machine (CMT6104) at room temperature, and the constant loading rate is 5×10^{-4}/s. Before that, specimen surfaces were carefully ground with the 1000# SiC

Table 1
Composition (wt. %) of investigated alloys.

	Alloy	Mg	Zn	Cu	Si	Mn	Cr	Fe	Al
1#	5083	4.52	0.23	0.09	0.42	0.57	0.15	0.42	Bal.
2#	5083-2%Zn	4.36	2.0	0.08	0.41	0.56	0.14	0.41	Bal.
3#	5083-4%Zn	4.24	4.0	0.08	0.38	0.54	0.13	0.39	Bal.
4#	5083-6%Zn	4.05	6.0	0.07	0.36	0.51	0.10	0.37	Bal.
5#	5083-6%Zn–3%Cu	3.81	6.0	3.0	0.36	0.50	0.10	0.37	Bal.
6#	5083-6%Zn–6%Cu	3.57	6.0	6.0	0.35	0.53	0.09	0.36	Bal.

paper and cleaned with alcohol by an ultrasonic cleaner. The sample dimension for tensile tests was shown in Fig. 1.

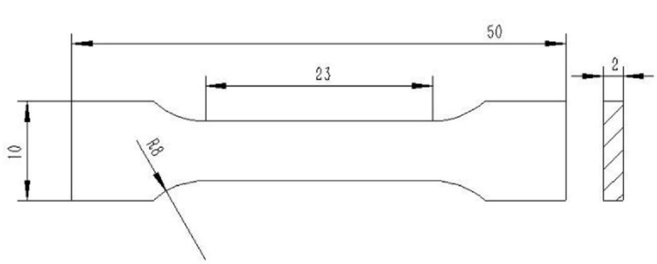

Fig. 1. Shape and size of the tensile specimens.

3. Results

3.1. Microstructure description

Fig. 2 shows the XRD analysis of the alloys. It can be seen from the figure that in the 5083 and the 5083-*x*wt.% Zn alloy, only the diffraction peak of α-Al can be obtained, which indicates that Mg and Zn are dissolved in the matrix. When Cu is added, the diffraction peak of the Al_2CuMg phase appears in the alloys, indicating that most of the Cu element forms the S-phase (Al_2CuMg).

Fig. 3 presents the scanning electron microscope (SEM) and the energy-dispersive X-ray spectroscope (EDS) analysis for the alloys. For the 5083 and 5083-*x*%Zn alloys, the precipitate phase with the high Fe content still exists in the alloy after the heat treatment, and no $MgZn_2$ phase is found in the 5083-*x*%Zn alloys, as presented in Fig. 3(a)–(d). Other elements, such as Mg, Mn, Zn etc., are evenly distributed in the alloy. The excessive Fe content will reduce the strength and ductility of the alloy. After the solution treatment, the content of Fe-rich phases in the 5083-6%Zn-*x*%Cu alloys is reduced, and the EDS results indicate that Mg and Zn are solved thoroughly into the matrix. Similarly, no $MgZn_2$ phase is found in the 5083-6% Zn-*x*%Cu alloy, and the undissolved S-phase (Al_2CuMg) is present in the matrix.

Figs. 4 and 5 show the EBSD mappings and grain-size distributions of three alloys. The microstructures of all alloys subjected to the aging heat treatment are the recrystallized equiaxed structures, which indicates that they all exhibit dynamic recrystallization. From the grain-size statistics chart, the grain sizes of the alloys are all between 10 and 20 μm. After adding 2% Zn, the grain size of the alloy is increased, compared to the 5083 aluminum alloy. When 4% and 6% Zn is continuously added, the grain size is reduced, even smaller than the 5083 aluminum alloy. Adding the 3% Cu to the 5083-6% Zn alloy finds that the grain size of the alloy is about 33 μm, but the grain size of the alloy is significantly reduced after adding 6% Cu. The grain size will be the important factor affecting the mechanical properties of the alloys.

Fig. 6 shows the fracture morphology of the alloys after tensile testing. There are a great number of deep dimples on the fracture of the 5083 aluminum alloy, indicating that the alloy has good plasticity and undergoes the ductile fracture. After adding 2 wt% - 6 wt% Zn, the number of dimples on the tensile fracture of the alloy decreases, and the depth of the dimple becomes shallow. Meanwhile, many brittle-fracture surfaces appear on the fracture of the alloys, which indicates that ductile and brittle fractures all exist in the alloys. When 3 wt% and 6 wt% Cu are added, obvious dimples are still observed in the fracture of the alloy. However, there are many small particles in the dimples, resulting in poor plasticity of the alloy.

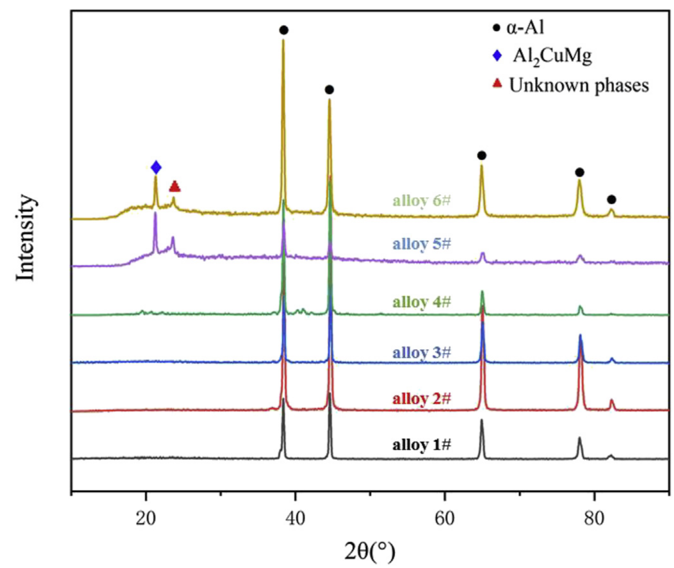

Fig. 2. X-ray diffraction patterns of alloys (1#:5083; 2#:5083-2%Zn; 3#:5083-4%Zn; 4#:5083-6%Zn; 5#:5083-6%Zn–3%Cu; 6#:5083-6%Cu–6%Zn).

3.2. Microhardness and dislocation density

Vickers microhardness (HV) was measured on the plane parallel to the longitudinal axis (rolling direction) by applying a load of 200 g for 15 s. The hardness values of the six alloys are shown in Fig. 7.

The hardness of the 5083 aluminum alloy is 122.3HV. When Zn is added, the hardness of the alloy increases to 167.8 HV. After adding 3% and 6% Cu, the hardness of the alloy is increased to 184.5HV, and the hardness value is increased by 50%, compared with the 5083 aluminum alloy. The increase in hardness is mainly attributed to the dislocation multiplication and interaction. Moreover, the precipitation of GP-zones and η-$MgZn_2$ or η′phases will also affect the hardness of the alloys [50,51].

The hardness values, retrieved from the indentation tests, increase with decreasing indentation depths [52]. This relationship is known as the indentation-size effect (ISE). The ISE results from an increase in the density of the geometrically-necessary dislocations required to accommodate the plastic deformation gradient around the indentation [53]. The dislocation density can be estimated from the microhardness value by Ref. [3]:

$$\rho = \frac{HV^2}{27\alpha^2 G^2 b^2} - \frac{3\sqrt{2}\sqrt{HV}\cot\phi}{\sqrt{1.72}\pi^2 b\sqrt{F}} \tag{1}$$

where HV is the Vickers hardness, ϕ is the slant angle of Vickers indenter (equal to 68°), α is an empirical constant with a value range for metal alloys between 0.2 and 0.5, G is the shear modulus of the aluminum alloy (26 GPa), F is the load of the Vickers indenter (200 g), and b is the Burgers vector of the dislocation (0.286 nm). Through the calculation of the above formula, the dislocation densities of the six alloys are 7.53×10^8, 11.54×10^8,13.22×10^8, 16.76×10^8, 17.41×10^8 and 20.93×10^8 (m^{-2}). Consistent with the trend of hardness, the density of dislocations also increases.

3.3. Mechanical properties

Through the tensile tests, the stress-strain curves of six different alloys were obtained, as shown in the figures Fig. 13below. With the

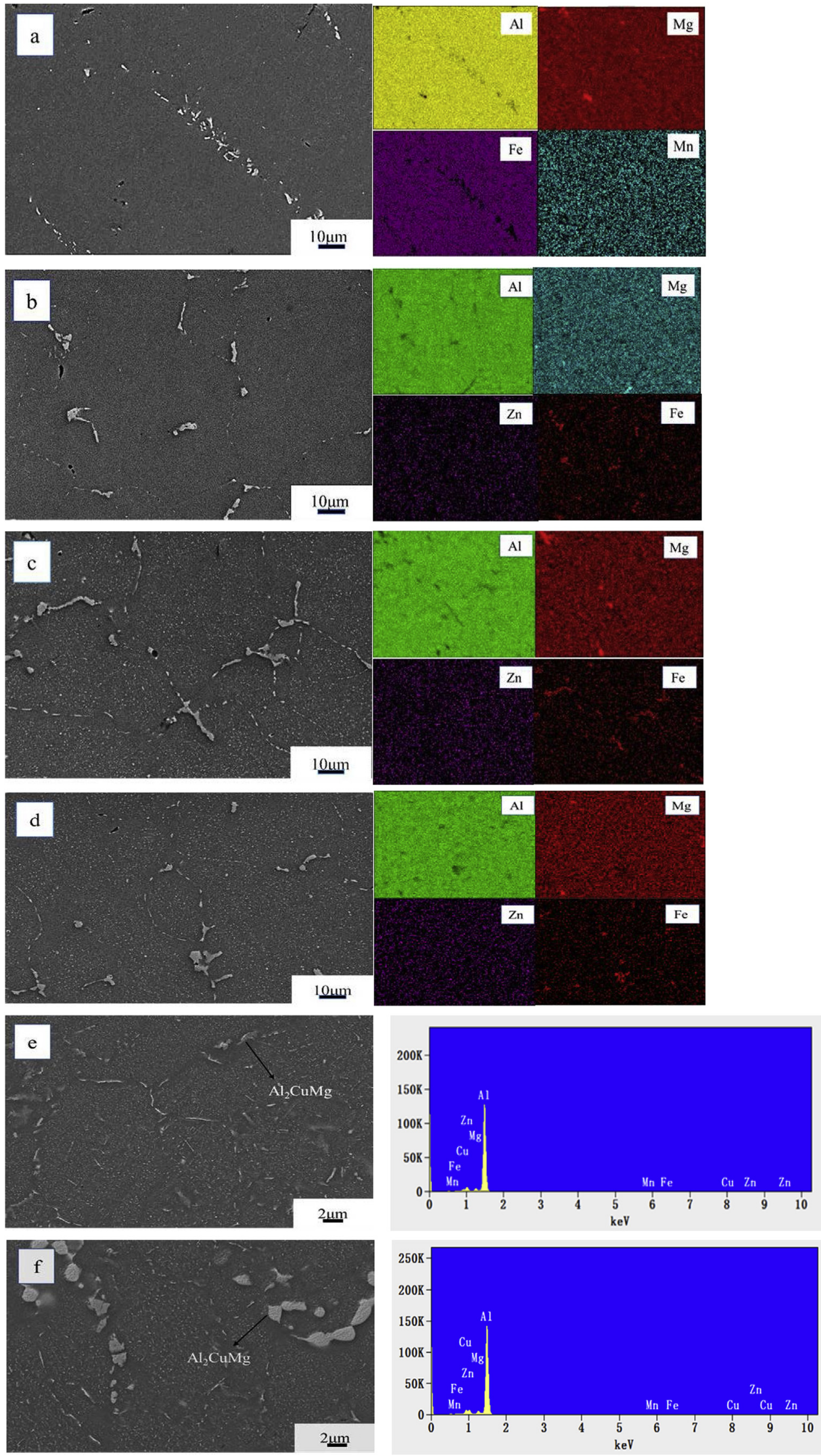

Fig. 3. The SEM and EDS analysis for the samples: (a) 5083 aluminum alloy; (b) 5083-2%Zn; (c) 5083-4%Zn; (d) 5083-6%Zn; (e) 5083-6%Zn−3%Cu; (f) 5083-6%Zn−6%Cu.

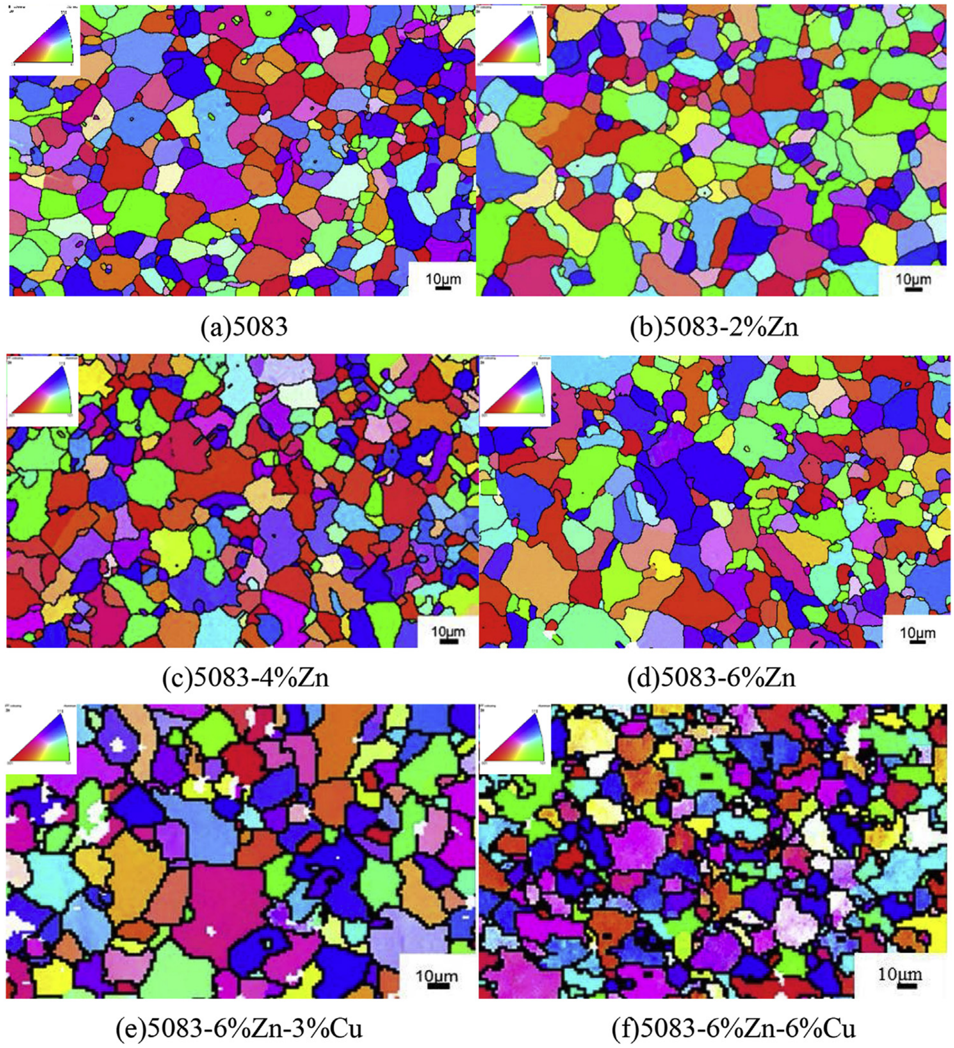

Fig. 4. EBSD mapping of the samples.

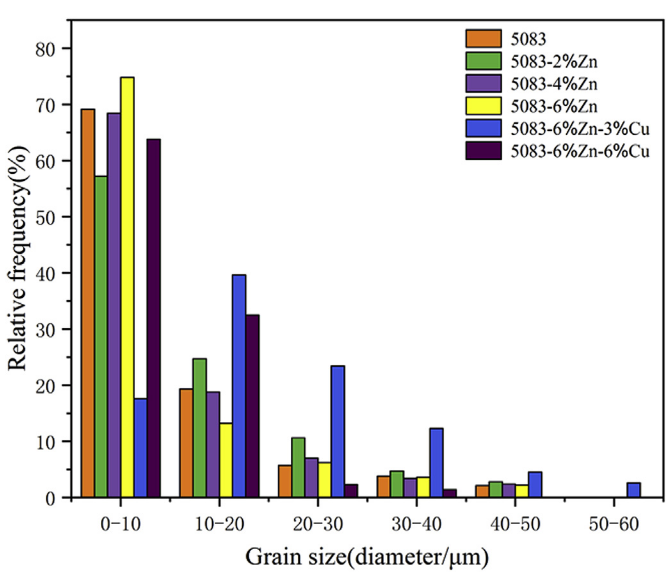

Fig. 5. The grain-size distributions of alloys.

addition of Zn and Cu elements, the tensile strength of the alloy increases continuously, from 189 MPa to 496 MPa, and the yield strength also increases from 86 MPa to 423 MPa. The elongation of the 5083 aluminum alloy is about 23%. When the Zn element is added, the elongation of the alloy decreases remarkably. When 3 wt % Cu is added, the elongation of the alloy is 6%, which is 74% lower than the 5083 aluminum alloy. However, it can be seen from the figure that when the content of Cu is increased to 6%, the plasticity of the alloy is effectively improved.

Compared with the 5083 aluminum alloy, the tensile strength of 5083-*x*%Zn alloys and 5083-6%Zn-*x*%Cu alloys increased by 12%, 17%, 34%, 139%, and 162% respectively. The main reason for the increase in strength is the grain refinement, solid-solution strengthening, and precipitation strengthening. In Zn-modified 5083 aluminum alloys, the main precipitates were the η-phase ($MgZn_2$) and τ-phase [$Mg_{32}(Al, Zn)_{49}$], featuring a hexagonal structure, which improves the strength of the alloys. The XRD analysis shows that both Zn and Mg are dissolved in the matrix, which acts as a solid solution for the alloy. The addition of the Cu element to the 5083-6% Zn alloy forms the S-phase (Al_2CuMg) in the alloy, which increases the strength of the alloy. Furthermore, the Cu element has a certain solubility in the η-phase ($MgZn_2$), which can reduce the potential difference between the matrix and the grain boundary, which can effectively improve the corrosion

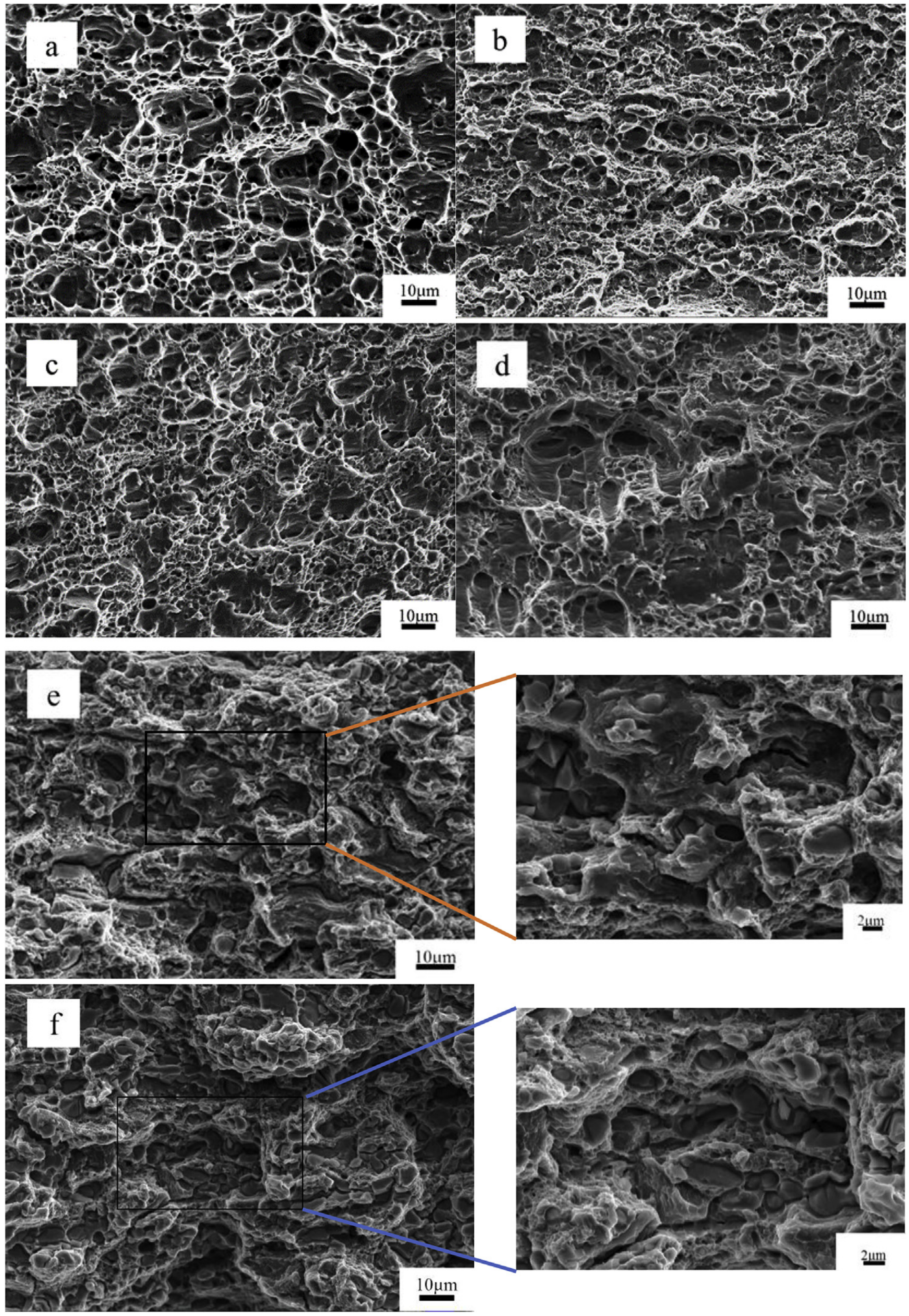

Fig. 6. The fracture morphology of alloys: (a) 5083 aluminum alloy; (b) 5083-2%Zn; (c) 5083-4%Zn; (d) 5083-6%Zn; (e) 5083-6%Zn–3%Cu; (f) 5083-6%Zn–6%Cu.

resistance of the alloy. It can be seen from the stress-strain curve that the additions of 3% and 6% Cu improve the mechanical properties of the alloys. The main reason is that the addition of Cu reduces the grain size of the alloy, and Cu can increase the dispersion of precipitates in the crystal and improve the precipitation phase of the grain boundary, which improve the plasticity of the alloys [54].

3.4. Serration characteristics

The tensile test was carried out at a strain rate of 5×10^{-4}/s, and the stress-strain curves of the six different alloys were obtained. It can be seen from the figures that different types of serrations appear on the stress-strain curve of the 5083-aluminum alloy, and with the additions of Zn and Cu elements, the serration on the stress-strain curve of the alloy gradually diminishes or even disappears.

It can be seen from the figure that the types of serrations exhibited by alloys with various compositions are very different, and the alloys of the same composition display different types of serrations under different strains. According to the degree of the serration density and the change of the stress amplitude, the serration can be divided into Types A, B, C, D, and E (see Fig. 11). Types A, B, and C are well-known, and their characteristics are also well documented. The A-type serration has a small change in the

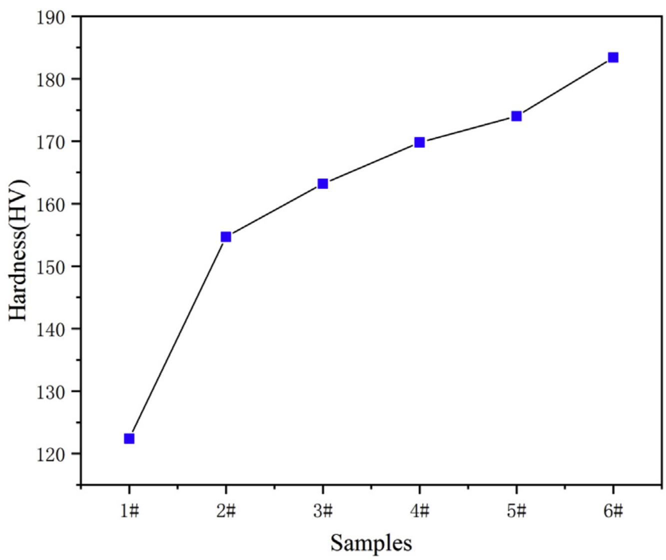

Fig. 7. Vickers hardness of the samples (1#:5083; 2#:5083-2%Zn; 3#:5083-4%Zn; 4#:5083-6%Zn; 5#:5083-6%Zn−3%Cu; 6#:5083-6%Cu−6%Zn).

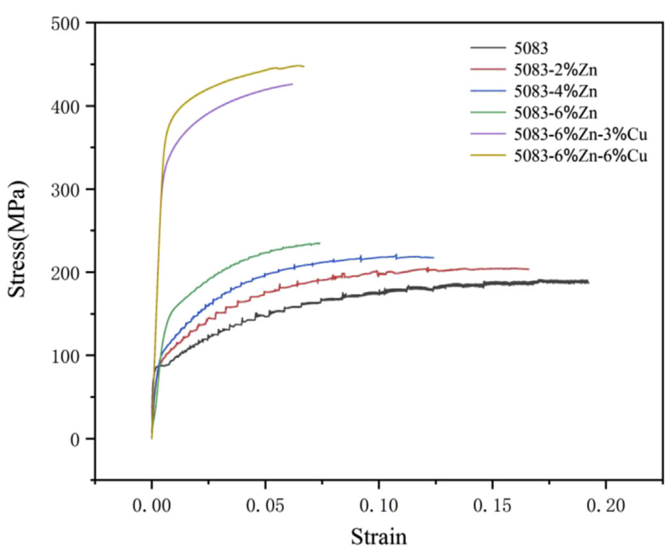

Fig. 8. Stress-strain curve of the samples.

stress amplitude and a large serration spacing. Conversely, the magnitude of the stress of the C-type serration varies greatly, and the serration is denser. The type of serrations between Types A and C is B-type. When the alloy is deformed to a certain extent, the diffusion rate of the solid-solution atoms will meet the minimum requirement for effective pinning of the movable dislocations. At this time, the load will increase when the serrations are generated, resulting in the formation of the A or A + B type serration. When the solute atom has a faster diffusion rate or the movable dislocation movement rate is lower, the solute atom has sufficient time to spread around the dislocations and pin the dislocations. Therefore, the dislocations are pinned by the solute atoms at the beginning of the deformation. When the stress is gradually increased until the dislocation is removed from the pinning, the serration load is decreased, thereby forming the C-type serration [55,56].

For the 5083 aluminum alloy, when the deformation is just beginning, the dislocations are pinned and detached by the solute atoms. Therefore, the initial stage of serrations is A-type. When the deformation is to a certain extent, the diffusion rate of the solid-solution atoms gradually increases, and the dislocations are pinned at a certain moment. The load is constantly increasing, resulting in A + B and C types serration. When the 2% and 4% Zn elements are added, the serration behavior of the alloy is weakened. It can be seen from the partial enlargement that in the early stages of deformation, the serration type is D, when the deformation reaches a certain level, the serration type is B, and the amplitude of the serration is smaller than the 5083 aluminum alloy. When the 6 wt% Zn element is added, the serration type of the alloy is E during the entire deformation, and the serration amplitude becomes smaller. When the Cu element is added, the serration behavior of the alloy disappears. The main reason why the serration gradually weakens or even disappears is the increase in the precipitation phase and dislocation density. Serration behaviors occur when moving dislocations are hindered by solute atoms, forest dislocations, twins, etc. When the precipitation phase increases, the solute atoms in the alloy decrease, resulting in weakening of the pinning effect on dislocations. As the strain increases, the dislocation density and moving rate increase, making it easy to get rid of the solute atoms and continue to move forward, showing the smooth curve on the stress-strain curve. Therefore, the critical strain is increasing, compared to the 5083 aluminum alloy (see Fig. 9).

There are two parameters to characterize the serration behavior of the alloys (Fig. 12) [57]. The stress drop of serrations ($\triangle\sigma$) is the stress difference between the highest and lowest points of the adjacent serration, and the reloading time of serrations ($\triangle t$) is the time that it takes for the serration to rise from the lowest point to the next highest point. These two parameters can intuitively describe the evolution of the serration behavior of the alloys. The figure below shows the distribution information of stress drop ($\Delta\sigma$) and reloading time (Δt) for different alloys at each segment. We divide the stress-strain curves of Fig. 10 into three segments of a, b, and c (see Fig. 13) .

Table 2 calculates the average stress drop and average reloading time of each segment. The average size of stress drops and reloading time are small at the segment-a but largest at the segment-b. On the whole, the stress drop ($\Delta\sigma$) of the 5083

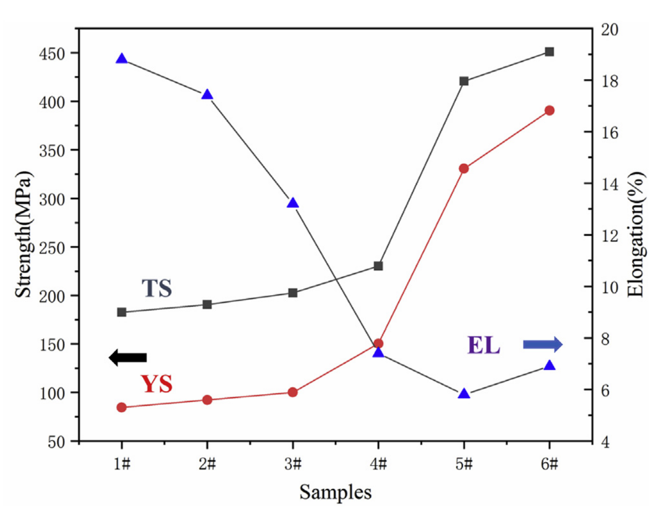

Fig. 9. Mechanical properties of the samples (1#:5083; 2#:5083-2%Zn; 3#:5083-4%Zn; 4#:5083-6%Zn; 5#:5083-6%Zn−3%Cu; 6#:5083-6%Cu−6%Zn).

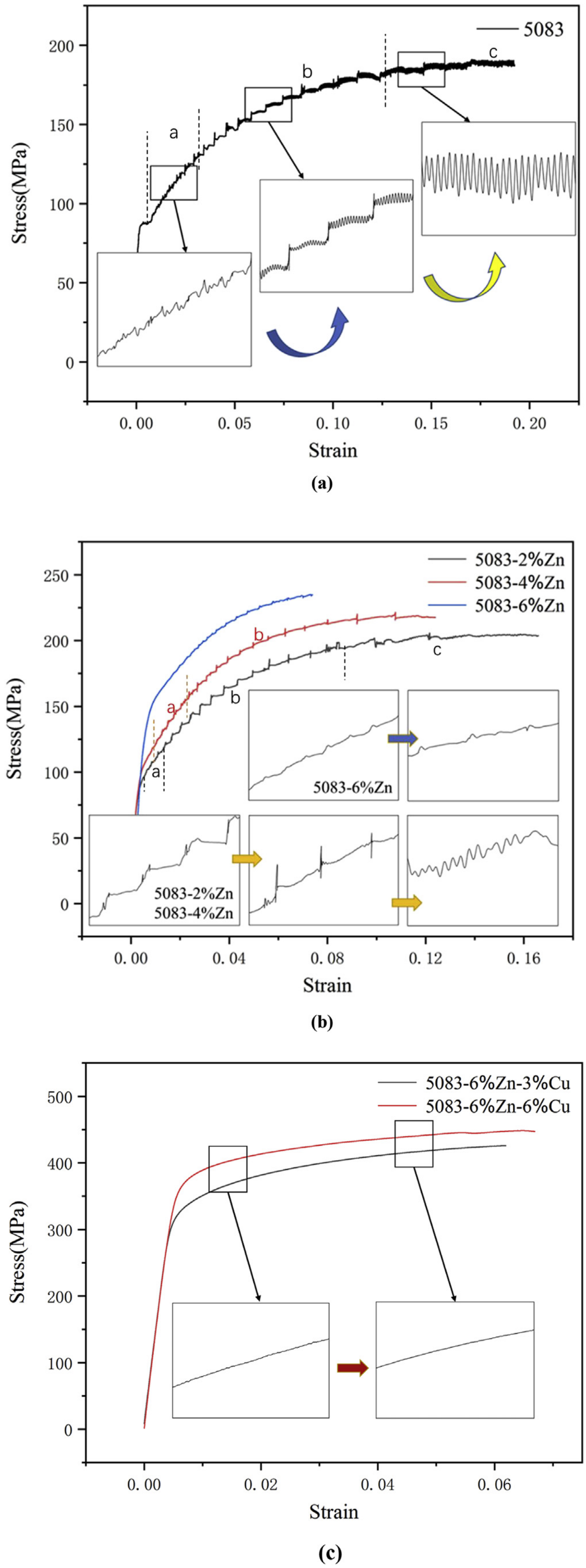

Fig. 10. Serration behavior of alloys.

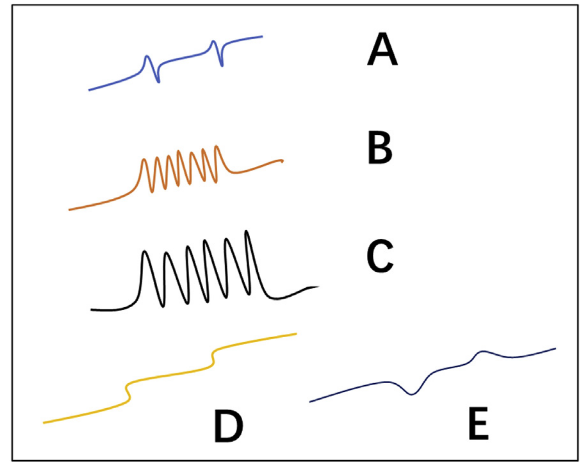

Fig. 11. Types of serrations.

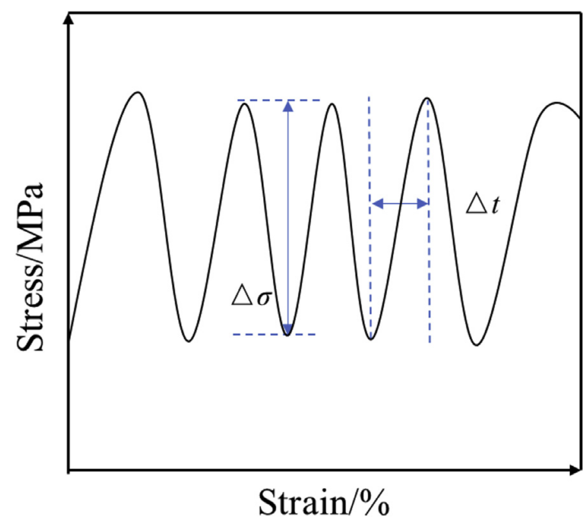

Fig. 12. Definition of $\triangle\sigma$ and $\triangle t$ in an enlarged stress-strain curve.

aluminum alloy is the largest, and with the increase of the Zn content, the stress drop is gradually reduced, indicating that the serration behavior of the alloy is gradually weakened. The type of serrations can be judged from the correspondence between the stress drop and reloading time. For example, the segment-a of the 5083 aluminum alloy has the smaller amplitude of stress drops and shorter reloading time, which indicates a Type-A serration. The $\triangle\sigma$ and $\triangle t$ increase simultaneously at the segment-b, which is the A and A + B types serration. The segment-c has a relatively-larger amplitude of stress drops but shorter reloading time, indicating the Type-C serration.

Among the different component alloys, the content of Mg in the 5083 aluminum alloy is the highest. According to the DSA theory (Please give references), as the solid-solution atom, the interaction of the Mg and dislocation will affect the serration behavior of the materials. When the Mg content is increased, the pinning effect of the solute atoms on the dislocations enhances, and the energy required for dislocations to get rid of the hindrance increases. Thus, the higher $\triangle\sigma$ and longer $\triangle t$ are observed in the stress-strain curve for the alloy with the greater Mg content, which is consistent with the trend of the obtained processing parameters. For other alloys, although different alloying elements are added, most of them exist in the form of precipitated phases. Moreover, at the

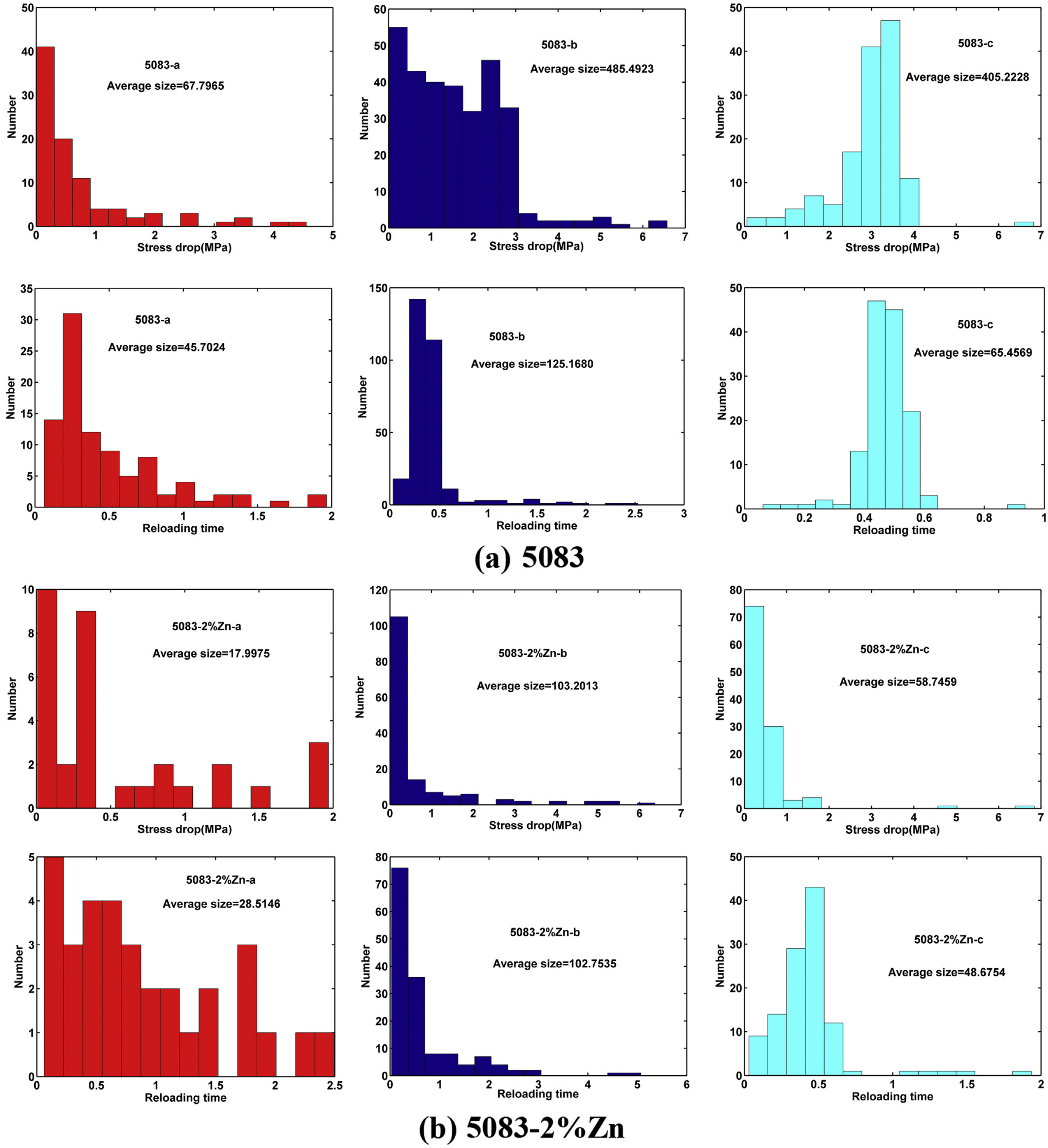

Fig. 13. The distribution information of stress drop ($\Delta\sigma$) and reloading time (Δt) for different alloys at each segment.

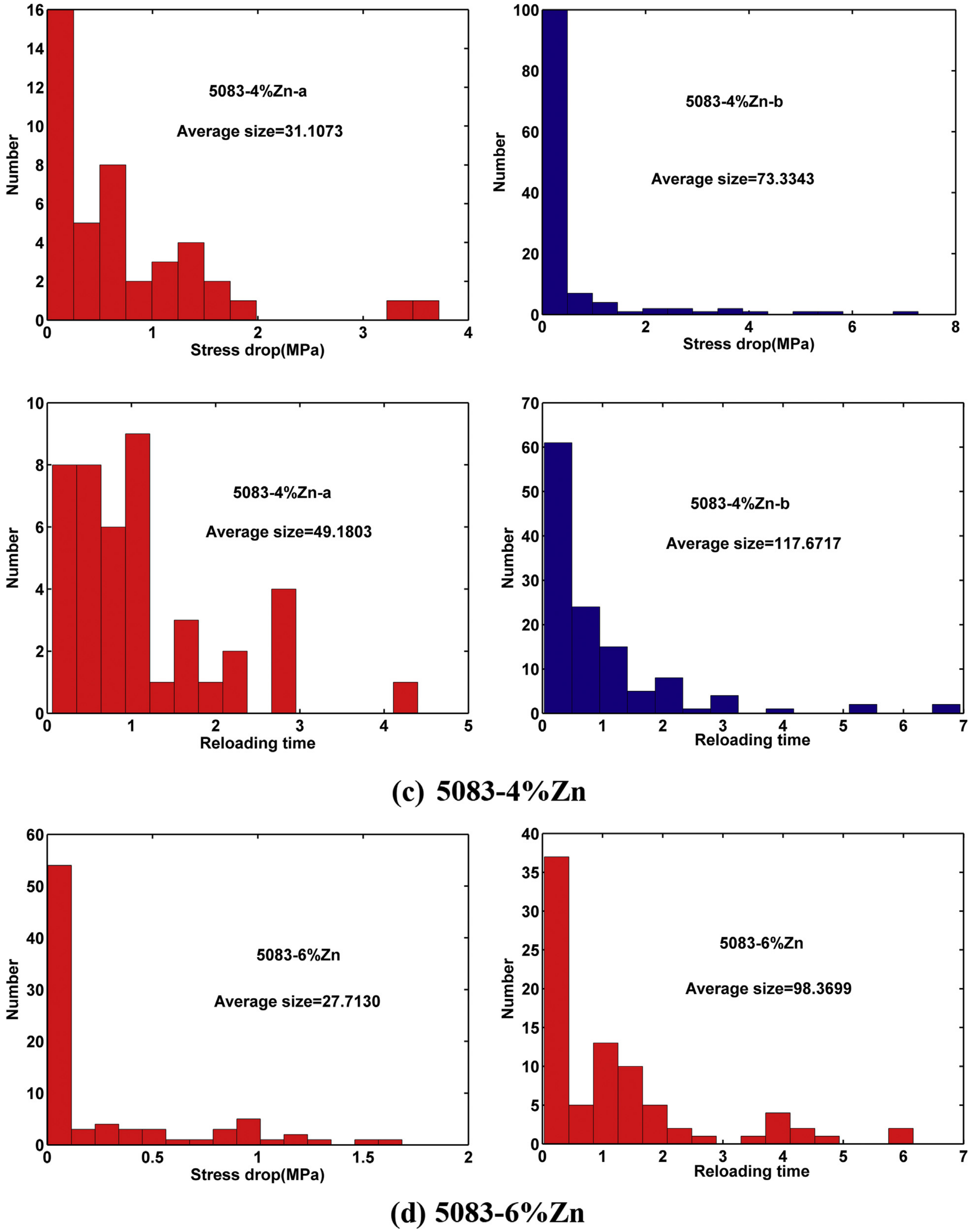

Fig. 13. (*continued*).

initial stage of the plastic deformation, due to the low dislocation density and the slow diffusion rate of solute atoms, the stress drop on the stress-strain curve are relatively small. The addition of Cu will form the S-phase (Al_2CuMg) in the alloy, which reduce the content of solute atoms, resulting in the weakening of the hindrance to dislocations. Therefore, the serration behavior of the alloys weaken or even disappear.

Table 2
The average size of stress drops and reloading time.

	Stress drop ($\Delta\sigma$/MPa)	Reloading time (Δt/s)
5083-a	67.79	45.70
5083-b	485.49	125.16
5083-c	405.22	65.45
5083-2%Zn-a	17.99	28.51
5083-2%Zn-b	103.20	102.75
5083-2%Zn-c	58.74	48.67
5083-4%Zn-a	31.10	49.18
5083-4%Zn-b	73.33	117.67
5083-6%Zn	27.71	98.36

Table 3
The calculated results of time delay, embedding dimension, and the largest Lyapunov exponent of different alloys.

	Time delay	Embedding dimension	Largest Lyapunov Exponent (λ)
5083	11	11	0.0027
5083-2%Zn	56	5	0.0010
5083-4%Zn	26	6	0.0012
5083-6%Zn	11	5	0.0010
5083-6%Zn−3% Cu	10	5	−0.0049
5083-6%Zn−6% Cu	5	5	−0.0047

4. Discussion

According to the results of XRD and EDS analyses, the addition of Zn and Cu elements changes the type of precipitated phases in the alloys. The mechanical properties of the alloys are improved due to the solid-solution strengthening and grain refinement.

The additions of Zn and Cu elements change the serration behavior of the alloys. Since most of Mg, Zn, and Cu elements exist in the form of precipitated phases, the number of solute atoms is reduced, and the pinning effect on dislocations is weakened, so the serration behavior is gradually weakened or even disappeared. Due to the change in the strain level, the same alloy exhibits different serration types on the stress-strain curve. To investigate the dynamic evolution of the serration, the one-dimensional serrated signal, $S = \{s(i), \quad i = 1, 2, \cdots, N\}$ was reconstructed into a high-dimensional phase space, denoted by Y.

$$Y = \begin{pmatrix} s(1) & s(2) & \cdots & s(N-(m-1)\tau) \\ s(1+\tau) & s(2+\tau) & \cdots & s(N-(m-2)\tau) \\ \vdots & \vdots & \vdots & \vdots \\ s(1+(m-1)\tau) & s(2+(m-1)\tau) & \cdots & s(N) \end{pmatrix}. \tag{2}$$

Here, τ is the time delay, and m is the embedding dimension (i.e., the dimension of the reconstructed phase space). The dynamic evolution of serrations can be characterized by the evolution of trajectories in reconstructed phase space according to the Takens embedding theorem [58,59].

The selection of the optimal time delay and embedding dimension is the key to reconstruct Y. In this paper, the optimal time delay, τ_0, is calculated by a mutual information technique [60]. The selection of an optimal embedding dimension is based on the Cao method [61]. After that reconstruction, the largest Lyapunov exponent (λ), which is a significant parameter for characterizing the dynamic behaviors of the trajectories in phase space, is calculated by the Wolf's method [62].

In the reconstructed phase space, an initial point and its nearest neighbor point are given as $Y(i_0)$ and $Y^*(i_0)$, and the distance between these two points is $d_0 = |Y(i_0) - Y^*(i_0)|$. Tracking the evolution from i_0 to i_1, $Y(i_0)$ evolves to $Y(i_1)$, and $Y^*(i_0)$ reaches $\tilde{Y}(i_1)$, and the distance, d_0, changes to $d_0^{'} = |Y(i_1) - \tilde{Y}(i_1)|$. While the point, $\tilde{Y}(i_1)$, may not be the nearest neighbor point of $Y(i_1)$ at the time, i_1. Hence, the nearest neighbor point of $Y(i_1)$ is reselected as $Y^*(i_1)$. The distance between $Y(i_1)$ and $Y^*(i_1)$ becomes $d_1 = |Y(i_1) - Y^*(i_1)|$. Then, tracking the evolution to i_2, we can obtain $d_1^{'} = |Y(i_2) - \tilde{Y}(i_2)|$ and $d_2 = |Y(i_2) - Y^*(i_2)|$. Repeating above process until the end of time series, we can determine the number of

Table 4
The calculated results of the time delay, embedding dimension, and largest Lyapunov exponent for each segment of strain-stress curves.

	Time delay	Embedding dimension	Largest Lyapunov exponent (λ)
5083-a	10	6	0.0012
5083-b	11	11	0.0016
5083-c	12	10	0.0049
5083-2%Zn-a	12	5	0.0014
5083-2%Zn-b	15	9	0.0010
5083-2%Zn-c	13	10	0.0039
5083-4%Zn-a	10	5	0.0015
5083-4%Zn-b	22	5	0.0068

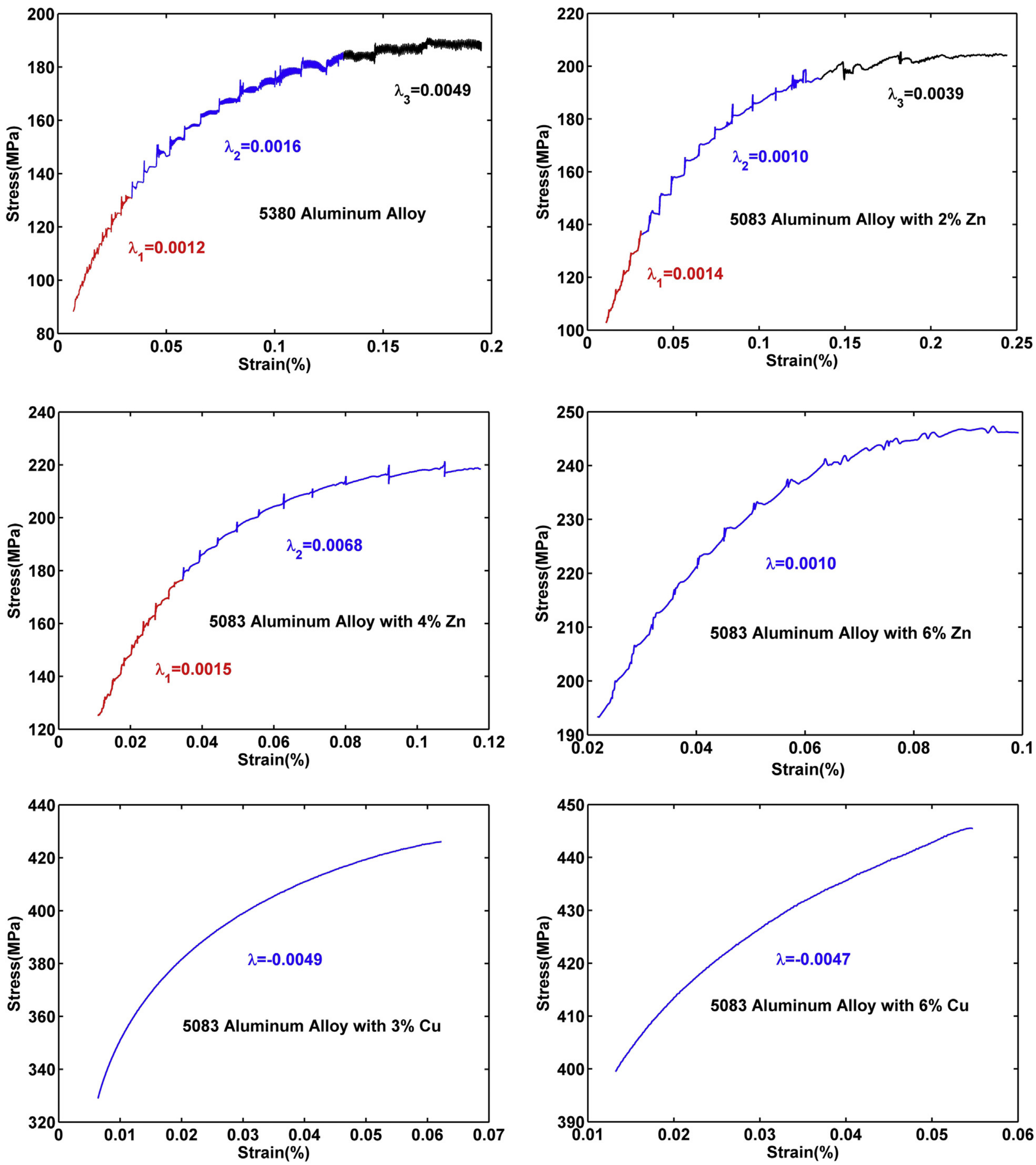

Fig. 14. The segmented serrations and its largest Lyapunov exponent.

these iterations as K. From the above process, we have $d_k = |Y(i_k) - Y^*(i_k)|$, and $d_k^{'} = |Y(i_k) - \tilde{Y}(i_k)|$, $k = 0, 1, 2, \cdots, K$. The largest Lyapunov exponent is defined as

$$\lambda = \frac{1}{i_K - i_0} \sum_{k=0}^{K} ln\left(d_k^{'} / d_k\right). \tag{3}$$

The values of the time delay, embedding dimension, and largest Lyapunov exponent of different alloys are listed in Table 3. It shows that the addition of Zn or Cu will decrease the value of the largest Lyapunov exponent, λ. The decreasing trend of λ reflects a weakness of instability. Particularly, the largest Lyapunov exponents of 5083−6%Zn−3%Cu and 5083-6%Zn−6%Cu are negative.

Furthermore, the largest Lyapunov exponent of segmented serrations are calculated. The corresponding results are shown in Table 4 and Fig. 14. We find the largest Lyapunov exponent of segment-a and segment-b are near to 0.0014±0.0003, while the largest Lyapunov exponent of segment-c is near triple larger than that of segment-a or segment-b.

We also study the serrated flow by using the refined composite

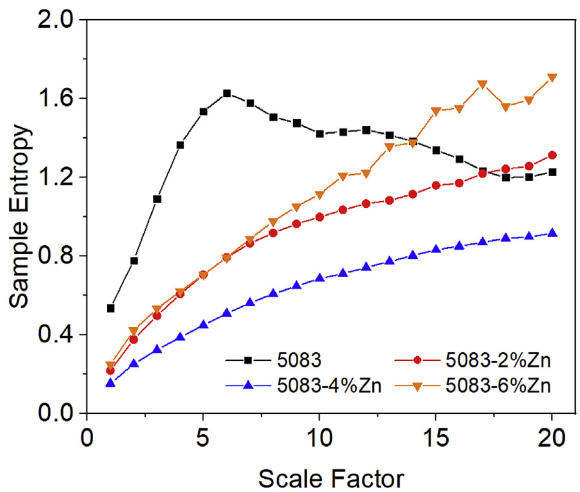

Fig. 15. The complexity analysis results for the 5083 aluminum alloy with varying amounts of Zn (0–6 wt %).

multiscale entropy algorithm. To begin the analysis, one first creates the coarse-grained series, which is written as [63]:

$$y^{\tau}_{k,j} = \frac{1}{\tau}\sum_{i=(j-1)\tau+k}^{j\tau+k-1} x_i; \quad 1 \le j \le \frac{N}{\tau} \quad 1 \le k \le \tau \tag{4}$$

here x_i is the ith point from the original time-series data, N is the total number of point of the original time series, τ is the scale factor, and k is an indexing factor that indicates at which point in the series to initialize the algorithm. The scale factor is essentially the number of data points that one averages over when creating Eq. (4). It should be noted that before applying Eq. (4), the underlying trend of the dynamic strain aging data must be omitted via polynomial or moving average methods [64]. From the Eq. (4), one next evaluates the template vectors, y^{τ}_{k}:

$$\boldsymbol{y^{\tau,m}_{k,i}} = \left\{ y^{\tau}_{k,i} \ y^{\tau}_{k,i+1} \ \ \ldots \ y^{\tau}_{k,i+m-1} \right\} \ ; \quad 1 \le i \le N-m; \ 1 \le k \le \tau \tag{5}$$

in general, m is typically set to 2 [46]. Next solve for the infinity norm, $d^{\tau,m}_{jl}$ [65]:

$$d^{\tau,m}_{jl} = \left\| \boldsymbol{y^{\tau,m}_{j}} - \boldsymbol{y^{\tau,m}_{l}} \right\|_{\infty} = \max\left\{ \left| y^{\tau}_{1,j} - y^{\tau}_{1,l} \right| \ldots \left| y^{\tau}_{i+m-1,j} - y^{\tau}_{i+m-1,l} \right| \times \right\} < r \tag{6}$$

here r is a tolerance value typically set to 0.15 times the standard deviation of the detrended data set [66]. The infinity norm is used to determine the number of matching vectors in the series. In this context, vectors match when the difference between their components are smaller than r, as defined above. Subsequently, one repeats this process for vectors of size, m + 1. Now one the total number of matching vectors of sizes m and m + 1, which will be denoted as n. From the total number of matching vectors one can determine the RCMSE value, which is typically denoted as the sample entropy for the given time series, and can be found from the following equation:

$$RCMSE(\boldsymbol{X}, \tau, m, r) = Ln\left(\frac{\sum_{k=1}^{\tau} n^{m}_{k,\tau}}{\sum_{k=1}^{\tau} n^{m+1}_{k,\tau}} \right) \tag{7}$$

The sample entropy is usually plotted as a function of the scale factor τ.

Fig. 15 displays the complexity results for the 5083 aluminum alloy with varying amounts of added Zn (2–6 wt %). The sample of 5083 exhibited the largest sample entropy values, as compared to the other specimens, for most of the scale factors. This result indicates that the sample exhibited the most complex serrations during tension testing. Furthermore, unlike the rest of the samples, the sample entropy values attained a maximum at $\tau = 6$. Except for the sample, which contained 6 wt % Zn, the complexity of the serrations appeared to decrease with an increasing amount of Zn in the sample. As for the specimen, which contained 6 wt % Zn, the sample entropy exhibited the largest values, as compared to the other samples, for $\tau > 14$. Furthermore, the sample entropy was higher for this condition, as compared to the samples, which contained lower amounts of Zn.

The results of the complexity analysis suggest the following trends for the samples, which contained less than 6 wt % Zn. The sample entropy curves generally increased in concert with the stress-drop magnitude, the grain size, the tensile and yield strengths, the degree of plasticity, and the solute density. On the other hand, the curves showed a decreasing trend with an increase in the Zn content, the hardness, and the dislocation density.

Importantly, this increase in the dynamical complexity of the serrated flow with an increase in the solute atom content is in agreement with the results reported in Ref. [44]. Thus, a greater amount of substitutional solute atoms are available to interact with mobile edge dislocations, leading to more complex serration behavior. The relatively-higher sample entropy values for the sample with 6 wt % Zn may be explained as follows. As the amount of Zn in the matrix increases, the number of dislocations also increase. The increase in the number of dislocations more than compensates for the loss of solute atoms, which results in a net increase in the number of interactions that can take place, leading to the serrated flow that exhibits more intricate behavior.

5. Conclusions

In this paper, the effects of Zn and Cu on the microstructures, mechanical properties, and serration behavior of the 5083 aluminum alloy were investigated. The main conclusions to be drawn from this study may be summarized as follows:

(1) The addition of Zn and Mg can change the grain size of the alloy. The alloy with 6% Cu has the smallest grain size.
(2) The strength, hardness, and dislocation density of the alloy increase with the additions of Zn and Cu. Among them, notably, Cu can not only improve the strength of the alloy, but also improve the plasticity of the alloy.
(3) Significant serration behavior is observed in the 5083 aluminum alloy, and the serration types are A, A + B and C. When the Zn element is added, the serration amplitude of the alloy is weakened, and the serration type is C. Especially when the Cu element is added, the serration behavior of the alloy disappears.
(4) With the additions of Zn and Cu alloy elements, the stress drop gradually decreases. The type of serration can also be judged by the correspondence between $\triangle\sigma$ and $\triangle t$, and the result of the judgment is consistent with the macroscopic representation of the stress-strain curve.
(5) The addition of Zn or Cu will decrease the value of the largest Lyapunov exponent, λ, indicating a weakness of instability. The largest Lyapunov exponents of 5083-6 wt%Zn-3wt.%Cu and 5083-6%wt.Zn-6%wt.Cu are negative, which indicates a

different dynamical evolution as compared to the other alloys.

(6) The complexity of the serrated flow increased with increasing the solute concentration, grain size, plasticity. This increase in the sample entropy was caused by an increase in the number of solute atom-dislocation line interactions that occur during the serration events.

Credit author statement

Zhang Bingbing: Methodology, Investigation, Writing - Original Draft.
Peter K. Liaw: Writing - Review & Editing.
Jamieson Brechtl: Formal analysis.
Ren Jingli: Writing - Review & Editing.
Guo Xiaoxiang: Formal analysis.
Zhang Yong: Conceptualization, Methodology, Supervision.

Declaration of competing interest

The authors declare that they have no known competing financial interests or personal relationships that could have appeared to influence the work reported in this paper.

Acknowledgements

Zhang Y. would like to thank the financial support from the National Natural Science Foundation of China (NSFC, 51471025 and 51671020). PKL very much appreciates the support of the U.S. Army Research Office project (W911NF-13-1-0438 and W911NF-19-2-0049) with the program managers, Drs. M. P. Bakas, S. N. Mathaudhu, and D. M. Stepp. PKL thanks the support from the National Science Foundation (DMR-1611180 and 1809640) with the program directors, Drs. G. Shiflet and D. Farkas.

References

[1] Tolga Dursun, Costas Soutis, Recent developments in advanced aircraft aluminium alloys, Mater. Des. 56 (2014).
[2] L. Kramer, M. Phillippi, W.T. Tack, C. Wong, Locally reversing sensitization in 5xxx aluminum plate, J. Mater. Eng. Perform. 21 (6) (2012).
[3] Jianchao Shi, Hongjie Luo, Yongliang Mu, Guangchun Yao, Effect of the addition of Zn on the microstructure and mechanical properties of 5083 alloy, J. Mater. Eng. Perform. 26 (6) (2017).
[4] T. Sheppard, N. Raghunathan, Modification of cast structures in Al-Mg alloys by thermal treatments, Mater. Sci. Technol. 5 (3) (1989) 268.
[5] J.B. Bessone, Mayer CE. SalinasDR, M. Ebert, W.J. Lorenz, An EIS study of aluminium barrier-type oxide films formed in different media, Electrochim. Acta 37 (1992) 2283–2290.
[6] Chunyan Meng, Di Zhang, Hua Cui, Linzhong Zhuang, Jishan Zhang, Mechanical properties, intergranular corrosion behavior and microstructure of Zn modified Al–Mg alloys, J. Alloy. Comp. (2014) 617.
[7] R.K. Gupta, C. Li, J. Xia, X. Zhou, G. Sha, B. Gun, Corrosion behavior of Al–4Mg–1Cu(wt%) microalloyed with Si and Ag, Mater. Sci. Technol. 17 (2015) 1670–1674.
[8] Waugh JLT. BergmanG, L. Pauling, The crystal structure of themetallic phase Mg32(Al, Zn)49, Acta Crystallogr. 10 (1957) 254–259.
[9] S.K. Maloney, K. Hono, I.J. Polmear, S.P. Ringer, The effects of a trace addition of silver upon elevated temperature ageing of an Al–Zn–Mg alloy, Micron 32 (2001) 741–747.
[10] Daokui Xu, Chuanqiang Li, Enhou Han, Lei Wang, Research Progress on the Plastic Instability Phenomenon of Metal Materials. Materials China, 2016.
[11] Luders W. Dingler's Polytechnisches J. 1860(5):18-22.
[12] A. Portevin, F. Le Chatelier, Comptes Rendus Hebd. Des Seances De L Acad. Des Sci. (Pairs) (177) (1925) 311–313.
[13] A.H. Cottrell, D.L. Dexter, Dislocations and Plastic Flow in Crystals, The Clarendon Press, 1956.
[14] A. Yilmaz, Temperature and surface potential correlations with serrated flow of low carbon steel, J. Mater. Sci. 46 (11) (2011) 3766–3776.
[15] Junying Min, Louis G. Hector Jr., Ling Zhang, Li Sun, John E. Carsley, Jianping Lin, Plastic instability at elevated temperatures in a TRIP-assisted steel, Mater. Des. 95 (2016) 370–386.
[16] Yong Zhang, Jun-wei Qiao, Peter K. Liaw, A brief review of high entropy alloys and serration behavior and flow units, J. Iron Steel Res. Int. 23 (1) (2016).
[17] C.-W. Tsai, C. Lee, P.-T. Lin, X. Xie, S. Chen, R. Carroll, M. LeBlanc, A. Braden, W. Brinkman, P.K. Liaw, K.A. Dahmen, J.-W. Yeh, Portevin-Le Chatelier mechanism in face-centered-cubic metallic alloys from low to high entropy, Int. J. Plast. (2019) 212–224.
[18] Yong Zhang, Jun Peng Liu, Shu Ying Chen, Xie Xie, Peter K. Liaw, Karin A. Dahmen, Jun Wei Qiao, Yan Li Wang, Serration and noise behaviors in materials, Prog. Mater. Sci. 90 (2017).
[19] Carroll Robert, Chi Lee, Tsai Che-Wei, Jien-Wei Yeh, Antonaglia James, A.W. Brinkman Braden, Michael LeBlanc, Xie Xie, Shuying Chen, K. Liaw Peter, A. Dahmen Karin, Experiments and model for serration statistics in low-entropy, medium-entropy, and high-entropy alloys, Sci. Rep. 5 (2015) 16997.
[20] J.P. Liu, X.X. Guo, Q.Y. Lin, Z.B. He, X.H. An, L.F. Li, P.K. Liaw, X.Z. Liao, L.P. Yu, J.P. Lin, L. Xie, J.L. Ren, Y. Zhang, Excellent ductility and serration feature of metastable CoCrFeNi high-entropy alloy at extremely low temperatures, Sci. China Mater. 62 (2019) 853.
[21] X.X. Guo, X. Xie, J.L. Ren, M. Laktionova, E. Tabachnikova, L.P. Yu, W.S. Cheung, K.A. Dahmen, P.K. Liaw, Plastic dynamic of the Al0.5CoCrCuFeNi high entropy alloy at cryogenic temperatures: jerky flow, stair-like fluctuation, scaling behavior, and non-chaotic state, Appl. Phys. Lett. (111) (2017), 251905.1.
[22] L.P. Yu, S.Y. Chen, J.L. Ren, Y. Ren, F.Q. Yang, K.A. Dahmen, P.K. Liaw, Plasticity performance of Al_0.5CoCrCuFeNi High-entrophy alloys under nano-indentation, J. Iron Steel Res. (24) (2017) 390–396.
[23] C. Chen, J.L. Ren, G. Wang, K.A. Dahmen, P.K. Liaw, Scaling behavior and complexity of plastic deformation for a bulk metallic glass at cryogenic temperatures, Phys. Rev. 92 (2015) 012113.
[24] J.L. Ren, C. Chen, G. Wang, W.S. Cheung, B.A. Sun, N. Mattern, S. Siegmund, J. Eckert, Various sizes of sliding event bursts in the plastic flow of metallic glasses based on a spatiotemporal dynamic model, J. Appl. Phys. (116) (2014) 033520.
[25] J.L. Ren, C. Chen, Z.Y. Liu, G. Wang, Plastic dynamics transition between chaotic and self-organized critical states in a glassy metal via multi-fractal intermediate, Phys. Rev. B (86) (2012) 134303.
[26] J.L. Ren, C. Chen, G. Wang, N. Mattern, J. Eckert, Dynamics of serrated flow in a bulk metallic glass, AIP Adv. (1) (2011) 032158.
[27] W. Wen, J.G. Morris, An investigation of serrated yielding in 5000 series aluminum alloys, Mater. Sci. Eng. A 354 (1–2) (2003) 279–285.
[28] Huifeng Jiang, Qingchuan Zhang, Yihao Xu, Xiaoping, Effect of aging on the serrated flow in Al-Cu alloys, Acta Metall. Sin. 42 (2) (2006) 139–142.
[29] Y.Z. Shen, K.H. Oh, D.N. Lee, The effect of texture on the Portevin–Le Chatelier effect in 2090 Al–Li alloy, Scr. Mater. 51 (4) (2004) 285–289.
[30] M.S. Bharathi, M. Lebyodkin, G. Ananthakrishna, C. Fressengeas, L.P. Kubin, Multifractal burst in the spatiotemporal dynamics of jerky flow, Phys. Rev. Lett. 87 (16) (2001) 4.
[31] M.S. Bharathi, M. Lebyodkin, G. Ananthakrishna, C. Fressengeas, L.P. Kubin, The hidden order behind jerky flow, Acta Mater. 50 (11) (2002) 2813–2824.
[32] T.A. Lebedkina, M.A. Lebyodkin, Effect of deformation geometry on the intermittent plastic flow associated with the Portevin–Le Chatelier effect, Acta Mater. 56 (2008) 5567–5574.
[33] T.A. Lebedkina, M.A. Lebyodkin, T.T. Lamark, M. Janeček, Y. Estrin, Effect of equal channel angular pressing on the Portevin–Le Chatelier effect in an Al3Mg alloy, Mater. Sci. Eng. 615 (2014) 7–13.
[34] M.A. Lebyodkin, Y. Bréchet, Y. Estrin, L.P. Kubin, Statistics of the catastrophic slip events in the Portevin–Le Châtelier effect, Phys. Rev. Lett. 74 (1995) 4758–4761.
[35] M.A. Lebyodkin, Y. Estrin, Multifractal analysis of the Portevin-Le Chatelier effect: general approach and application to AlMg and AlMg/Al2O3 alloys, Acta Mater. 53 (12) (2005) 3403–3413.
[36] M.A. Lebyodkin, N.P. Kobelev, Y. Bougherira, D. Entemeyer, C. Fressengeas, T.A. Lebedkina, I.V. Shashkov, On the similarity of plastic flow processes during smooth and jerky flow in dilute alloys, Acta Mater. 60 (2012) 844–850.
[37] M.A. Lebyodkin, T.A. Lebedkina, Multifractality and randomness in the unstable plastic flow near the lower strain-rate boundary of instability, Phys. Rev. 77 (2) (2008) 8.
[38] M.A. Lebyodkin, T.A. Lebedkina, Multifractal analysis of evolving noise associated with unstable plastic flow, Phys. Rev. 73 (3) (2006) 8.
[39] M.A. Lebyodkin, T.A. Lebedkina, A. Jacques, Multifractal Analysis of Unstable Plastic Flow, Nova Science Publishers, Inc., New York, 2009.
[40] J. Brechtl, S.Y. Chen, X. Xie, Y. Ren, J.W. Qiao, P.K. Liaw, S.J. Zinkle, Towards a greater understanding of serrated flows in an Al-containing high-entropy-based alloy, Int. J. Plast. 115 (2019) 71–92.
[41] S. Chen, L. Yu, J. Ren, X. Xie, X. Li, Y. Xu, G. Zhao, P. Li, F. Yang, Y. Ren, P.K. Liaw, Self-similar random process and chaotic behavior in serrated flow of high entropy alloys, Sci. Rep. 6 (2016) 29798.
[42] A. Sarkar, A. Chatterjee, P. Barat, P. Mukherjee, Comparative study of the Portevin-Le Chatelier effect in interstitial and substitutional alloy, Mater. Sci. Eng. A Struct. Mater. Prop. Microstruct. Process. 459 (1–2) (2007) 361–365.
[43] A. Sarkar, P. Barat, P. Mukherjee, Multiscale entropy analysis of the Portevin-Le Chatelier effect in an Al-2.5%Mg alloy, Fractals 18 (3) (2010) 319–325.
[44] J. Brechtl, B. Chen, X. Xie, Y. Ren, J.D. Venable, P.K. Liaw, S.J. Zinkle, Entropy modeling on serrated flows in carburized steels, Mater. Sci. Eng., A 753 (2019) 135–145.
[45] A. Sarkar, S.A. Maloy, K.L. Murty, Investigation of Portevin-LeChatelier effect in HT-9 steel, Mater. Sci. Eng. A 631 (2015) 120–125.

[46] M. Costa, A.L. Goldberger, C.K. Peng, Multiscale entropy analysis of biological signals, Phys. Rev. 71 (2) (2005) 021906.
[47] J.M. Reed, M.E. Walter, Observations of serration characteristics and acoustic emission during serrated flow of an Al–Mg alloy, Mater. Sci. Eng. A 359 (1–2) (2003) 1–10.
[48] S.P. Joshi, C. Eberl, B. Cao, K.T. Ramesh, K.J. Hemker, On the occurrence of Portevin–Le Châtelier instabilities in ultrafine-grained 5083 aluminum alloys, Exp. Mech. 49 (2) (2009) 207–218.
[49] T. Berstad, Effects of strain rate on the characteristics of PLC deformation bands for AA5083-H116 aluminium alloy, Philos. Mag. 88 (28–29) (2008) 3311–3338.
[50] X.P. Ding, H. Cui, J.X. Zhang, H.X. Li, M.X. Guo, Z. Lin, The effect of Zn on the age hardening response in an Al–Mg–Si alloy, Mater. Des. 65 (2015) 1229–1235.
[51] L. Hadjadj, R. Amira, The effect of Cu addition on the precipitation and redissolution in Al–Zn–Mg alloy by the differential dilatometry, J. Alloy. Comp. 484 (1–2) (2009) 0–895.
[52] S. Graça, R. Colaço, R. Vilar, Indentation size effect in nickel and cobalt laser clad coatings, Surf. Coat. Technol. 202 (3) (2007) 538–548.
[53] W.D. Nix, H. Gao, Indentation size effects in crystalline materials: a law for strain gradient plasticity, J. Mech. Phys. Solids 46 (3) (1998) 411–425.
[54] I.J. Polmear, A trace element effect in alloys based on the aluminum-zinc-magnesium system, Nature 186 (1960) 303–304.
[55] P. Rodriguez, Serrated plastic flow, Bull. Mater. Sci. 6 (4) (1984) 653–663.
[56] Baohui Tian, Huanxi Li, Yonggang Zhang, Changlin Chen, Generation mechanism of serration behavior in Al-Li single crystal, Acta Metall. Sin. 34 (6) (1998) 603–608.
[57] G. Saad, S.A. Fayek, A. Fawzy, et al., Serrated flow and work hardening characteristics of Al-5356 alloy, J. Alloy. Comp. 502 (1) (2010) 0–146.
[58] F. Takens, Detecting strange attractors in turbulence, Lect. Notes Math. 366 (1981).
[59] N.H. Packard, J.P. Crutchfield, J.D. Farmer, R.S. Shaw, Geometry from a time series, Phys. Rev. Lett. 45 (1980) 712.
[60] A.M. Fraser, H.L. Swinney, Independent coordinates for strange attractors from mutual information, Phys. Rev. A 2 (1986) 1134.
[61] L. Cao, Practical method for determining the minimum embedding dimension of a scalar time series, Phys. D Nonlinear Phenom. 110 (43) (1997).
[62] A. Wolf, J.B. Swift, H.L. Swinney, J.A. Vastano, Determining Lyapunov exponents from a time series, Phys. D Nonlinear Phenom. 16 (1985) 285.
[63] S.-D. Wu, C.-W. Wu, S.-G. Lin, K.-Y. Lee, C.-K. Peng, Analysis of complex time series using refined composite multiscale entropy, Phys. Lett. A 378 (2014) 1369–1374.
[64] A.C. Iliopoulos, N.S. Nikolaidis, E.C. Aifantis, Analysis of serrations and shear bands fractality in UFGs, J. Mech. Behav. Mater. 24 (1–2) (2015) 1–9.
[65] J. Brechtl, X. Xie, P.K. Liaw, S.J. Zinkle, Complexity modeling and analysis of chaos and other fluctuating phenomena, Chaos, Solit. Fractals 116 (2018) 166–175.
[66] M. Costa, A.L. Goldberger, C.K. Peng, Multiscale entropy analysis of complex physiologic time series, Phys. Rev. Lett. 89 (6) (2002) 068102.